Pole-zero analysis of scattering resonances of multilayered nanospheres

Yuyao Chen and Luca Dal Negro

Phys. Rev. B **98**, 235413 — Published 11 December 2018

DOI: 10.1103/PhysRevB.98.235413

Pole-Zero Analysis of Scattering Resonances of Multi-layered Nanospheres

Yuyao Chen[1] and Luca Dal Negro[1, 2, 3, *]

[1] *Department of Electrical and Computer Engineering and Photonics Center, Boston University, Boston, Massachusetts, 02215, USA.*
[2] *Division of Material Science and Engineering, Boston University, Boston, Massachusetts, 02215, USA.*
[3] *Department of Physics, Boston University, Boston, Massachusetts, 02215, USA*

We demonstrate a general pole-zero method for the design of the scattering resonances of multi-layered nanospheres and apply it to the relevant cases of strongly dispersive light scattering from metal-dielectric-metal and all-dielectric nanostructures. The pole-zero method is based on the full-wave iterative solution of the Mie scattering theory of multi-layered spheres, which is valid beyond the conventional quasi-static limit. By investigating scattering resonances in the complex frequency plane we show how to engineer anomalous Fano-like dipolar lineshapes from complex pole-zero interactions controlled by the geometrical parameters of the structures. The pole-zero method is then applied to the design of the back-scattering and forward scattering efficiencies beyond the dipolar approximation. The engineering of novel scattering and absorption resonances with customized lineshapes in metal-dielectric nanostructures provides unique opportunities for active devices including optical sensors, light emitters, and nonlinear elements.

PACS numbers: 42.25.Fx, 73.20.Mf, 41.20.Jb

I. INTRODUCTION

In 1961, Ugo Fano introduced a coupled resonance lineshape, now known as Fano resonance, which is characterized by its asymmetric profile and high Q value.[1] This coupled resonance has been studied widely in classical electrodynamics, with examples in finite clusters and photonic crystals,[2,3] metamaterials,[4,5] and plasmonic nanoparticles.[6,7] Recently, there has been a substantial effort in developing *ab-initio* theories for the rigorous understanding of Fano-like resonances in coupled electromagnetic nanostructures.[8,9] Furthermore, nanostructures with Fano lineshapes became attractive for applications to chemical and biological sensing[10,11] as well as electro-optics.[12,13] Fano lineshapes are not only observed in the scattering of multi-particle coupled nanostructures but also in single particles with an internal structure, such as core-shell[14] and, more generally, multi-layered nanoparticles.[15,16] In particular, the scattering spectra of the Au-SiO_2-Au nanospheres exhibit characteristic Fano lineshapes, which are known as dipole-dipole Fano-like resonances.[17] These resonances have often been discussed within a qualitative model that consists of three coupled oscillators.[17] However, it is difficult to precisely correlate the geometric parameters of the particles (core and shell radii) with the ones of the coupled oscillators. Furthermore, despite its intuitive appeal the three-oscillator model does not allow one to fully explain differential scattering spectra, such as the back-scattering and the forward-scattering efficiency spectra, which are contributed by the coherent interference of higher-order electromagnetic multipoles. Therefore, it is of interest to introduce a more general approach capable not only of unveiling the nature of Fano-like resonances in multi-layered nanostructures but also to precisely engineer the scattering lineshapes by tuning the structural parameters of the nanostructures.

In this work we leverage the full-vector iterative Mie solution of arbitrary multi-layered spheres and perform a rigorous pole-zero analysis of the dipolar Lorenz-Mie coefficients in the complex frequency plane. This approach unveils the nature of Fano-like resonances as general manifestations of pole-zero proximity interactions, beyond the quasi-static limit. In addition, it enables the predication of novel anomalous scattering lineshapes that appear when an additional pole with a large imaginary part overlaps a pole-zero pair. Our method is systematically applied to the Ag-SiO_2-Ag three-layered sphere system where we investigate how the modification of the geometric parameters affects the location of the poles and zeros in the complex frequency plane. By studying this relationship, we demonstrate the ability to engineer Fano-like resonances as well as to create novel anomalous scattering lineshapes resulting from more complex pole-zero interactions. Finally, we apply the pole-zero method to study the back-scattering efficiency (Q_{bs}) and the forward-scattering efficiency (Q_{fd}) of the Ag-SiO_2-Ag system and show that Q_{fd} can be strongly enhanced while Q_{bs} is simultaneously minimized due to the interaction with quadrupolar resonances. Finally, the flexibility of the pole-zero approach for the engineering of anomalous lineshapes is demonstrated by additionally applying it to the cases of Au-SiO_2-Au and fully dielectric Si-SiO_2-Si systems.

II. MIE THEORY OF MULTI-LAYERED SPHERES

Figure 1 shows a schematic of the three-layered sphere geometry used throughout the paper. The three geometric parameters r_1, d_2, d_3 are the radius of the metal core (Ag or Au), the thickness of the middle SiO_2 layer, and the thickness of the outer layer, respectively. On the

other hand, in the fully dielectric implementation of the multi-layered sphere system the inner and outer layers will be replaced by Si. The electromagnetic scattering

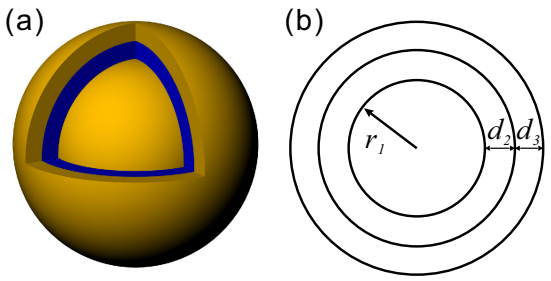

FIG. 1. (a) 3D view of the Ag-SiO_2-Ag three-layered sphere, (b) 2D cross section view and geometric parameters of the three-layered sphere

of light by core-shell spheres was studied by Bohren and Huffman[18] using the Mie scattering theory. Here the approach is extended to general m-layered spheres using the recursive algorithm described in reference[19] where $r_1, r_2, ...r_m$ denote the radii of concentric spheres with r_1 being the innermost sphere. Each layer has a refractive index $n_i(\omega) = \sqrt{\epsilon_i(\omega)\mu_i(\omega)}$ where $\epsilon_i(\omega)$ and $\mu_i(\omega)$ are respectively the relative permittivity and relative permeability of the i^{th} layer at the angular frequency ω. Here $i = 1, 2, ...m+1$, where $i = 1$ indicates the innermost layer and $i = m+1$ labels the host medium which is assumed to be non-absorbing (air in our case). Using the same definition of vector spherical harmonics $\mathbf{M}^k_{o1n}, \mathbf{M}^k_{e1n}, \mathbf{N}^k_{o1n}, \mathbf{N}^k_{e1n}$ provided in reference,[18] we express the incident plane wave traveling along the z-axis with electric field polarized along the x-axis as:

$$\mathbf{E}_{inc} = \sum_{n=1}^{\infty} E_n \left[\mathbf{M}^{(1)}_{o1n} - i\mathbf{N}^{(1)}_{e1n}\right] \tag{1}$$

$$\mathbf{H}_{inc} = -\frac{1}{\eta_{m+1}} \sum_{n=1}^{\infty} E_n \left[\mathbf{M}^{(1)}_{e1n} + i\mathbf{N}^{(1)}_{o1n}\right] \tag{2}$$

where $E_n = E_0 i^n \frac{2n+1}{n(n+1)}$ and E_0 is the incident plane wave electric field amplitude. The scattered and internal field expansions inside the i-layer are:

$$\mathbf{E}^{(i)}_{int} = \sum_{n=1}^{\infty} E_n \Big[c^{(i)}_n \mathbf{M}^{(1)}_{o1n} - i\tilde{c}^{(i)}_n \mathbf{N}^{(1)}_{e1n} + d^{(i)}_n \mathbf{M}^{(2)}_{o1n} - i\tilde{d}^{(i)}_n \mathbf{N}^{(2)}_{e1n}\Big] \tag{3}$$

$$\mathbf{H}^{(i)}_{int} = -\frac{1}{\eta_i} \sum_{n=1}^{\infty} E_n \Big[c^{(i)}_n \mathbf{M}^{(1)}_{e1n} + i\tilde{c}^{(i)}_n \mathbf{N}^{(1)}_{o1n} + d^{(i)}_n \mathbf{M}^{(2)}_{e1n} + i\tilde{d}^{(i)}_n \mathbf{N}^{(2)}_{o1n}\Big] \tag{4}$$

$$\mathbf{E}_{sca} = \sum_{n=1}^{\infty} \mathbf{E}_n \left[ia_n \mathbf{N}^{(3)}_{e1n} - b_n \mathbf{M}^{(3)}_{o1n}\right] \tag{5}$$

$$\mathbf{H}_{sca} = \frac{1}{\eta_{m+1}} \sum_{n=1}^{\infty} \mathbf{E}_n \left[ib_n \mathbf{N}^{(3)}_{e1n} + a_n \mathbf{M}^{(3)}_{o1n}\right] \tag{6}$$

The superscript i labels the parameters of the i^{th} layer ($i = 1, 2 \ldots, m$) and $\eta_i = \sqrt{\frac{\mu_o \mu_i}{\epsilon_o \epsilon_i}}$ is the impedance of the i^{th} layer while η_{m+1} is the one of free space. The Lorenz-Mie coefficients $a_n, b_n, c_n, d_n, \tilde{c_n}, \tilde{d_n}$ for the scattered and the internal fields are determined by applying the electromagnetic boundary conditions that require continuity of the tangential components of the E and H fields at each interface ($r = r_1, r_2, \ldots, r_m$). After some algebraic manipulations this process yields the following expressions for the scattering coefficients:

$$a_n = \frac{\psi_n(k_0 r_m) - R^{(m)}_E \psi'_n(k_0 r_m)}{\xi_n(k_0 r_m) - R^{(m)}_E \xi'_n(k_0 r_m)} \tag{7}$$

$$b_n = \frac{\psi_n(k_0 r_m) - R^{(m)}_H \psi'_n(k_0 r_m)}{\xi_n(k_0 r_m) - R^{(m)}_H \xi'_n(k_0 r_m)} \tag{8}$$

where $R^{(m)}_H$ and $R^{(m)}_E$ are calculated recursively using the following expressions:

$$\frac{d^{(i)}_n}{c^{(i)}_n} = \frac{\psi_n(k_i r_{i-1}) - R^{i-1}_H \psi'_n(k_i r_{i-1})}{\chi_n(k_i r_{i-1}) - R^{i-1}_H \chi'_n(k_i r_{i-1})} \tag{9}$$

$$\frac{\tilde{d}^{(i)}_n}{\tilde{c}^{(i)}_n} = \frac{\psi_n(k_i r_{i-1}) - R^{i-1}_E \psi'_n(k_i r_{i-1})}{\chi_n(k_i r_{i-1}) - R^{i-1}_E \chi'_n(k_i r_{i-1})} \tag{10}$$

$$R^{(i)}_H = \sqrt{\frac{\mu_i \epsilon_{i+1}}{\mu_{i+1} \epsilon_i}} \frac{\psi_n(k_i r_{i-1}) - \frac{d^{(i)}_n}{c^{(i)}_n} \chi_n(k_i r_i)}{\psi'_n(k_i r_{i-1}) - \frac{d^{(i)}_n}{c^{(i)}_n} \chi'_n(k_i r_i)} \tag{11}$$

$$R^{(i)}_E = \sqrt{\frac{\epsilon_i \mu_{i+1}}{\epsilon_{i+1} \mu_i}} \frac{\psi_n(k_i r_{i-1}) - \frac{\tilde{d}^{(i)}_n}{\tilde{c}^{(i)}_n} \chi_n(k_i r_i)}{\psi'_n(k_i r_{i-1}) - \frac{\tilde{d}^{(i)}_n}{\tilde{c}^{(i)}_n} \chi'_n(k_i r_i)} \tag{12}$$

In the equations above $k_i = \frac{\omega}{c_0} n_i(\omega)$ is the wave number in the i^{th} layer and the Riccati-Bessel functions ψ_n, χ_n, ξ_n are related to the spherical Bessel functions by $\psi_n(z) = z j_n(z)$, $\chi_n(z) = z y_n(z)$, and $\xi_n(z) = z h^1_n(z)$, while as usual the primes indicate differentiation with respect to the argument of the functions.

Due to the singularity of ξ_n at the origin, the initial conditions for Eqs. (9)-(12) are $\frac{d^{(1)}_n}{c^{(1)}_n} = 0, \frac{\tilde{d}^{(1)}_n}{\tilde{c}^{(1)}_n} = 0$. Consequently, we can calculate the coefficients a_n and b_n recursively starting from the innermost layer.

After obtaining a_n and b_n, the total scattering efficiency Q_{sca}, the total extinction efficiency Q_{ext}, the total absorption efficiency Q_{abs}, the back-scattering efficiency Q_{bs}, and the forward-scattering efficiency Q_{fd} of

the multi-layered sphere are computed according to the equations[18]:

$$Q_{sca} = \frac{2}{(k_0 r_m)^2}\sum_{n=1}^{\infty}(2n+1)(|a_n|^2+|b_n|^2) \quad (13)$$

$$Q_{ext} = \frac{2}{(k_0 r_m)^2}\sum_{n=1}^{\infty}(2n+1)\mathrm{Re}\{a_n+b_n\} \quad (14)$$

$$Q_{abs} = Q_{ext} - Q_{sca} \quad (15)$$

$$Q_{bs} = \frac{1}{(k_0 r_m)^2}\left|\sum_{n=1}^{\infty}(2n+1)(-1)^n(a_n-b_n)\right|^2 \quad (16)$$

$$Q_{fd} = \frac{1}{(k_0 r_m)^2}\left|\sum_{n=1}^{\infty}(2n+1)(a_n+b_n)\right|^2 \quad (17)$$

The series expansions above are truncated to order N according to the convergence criterion:

$$N = x + 4.05x^{1/3} + 2, \quad (18)$$

We considered the outer-most layer radius and the smallest wavelength to obtain the size parameter $x = \frac{2\pi}{\lambda}r_m$ for higher accuracy. For a multi-layered sphere with the outmost layer radius $r_m = 120nm, \lambda = 300nm$ we need to consider $N = 10$, which results in a relative truncation error[20] smaller than 10^{-15}.

III. SCATTERING EFFICIENCY SPECTRUM OF THREE-LAYERED SPHERES

We now apply the method outlined in Section II to study the scattering properties of the Ag-SiO_2-Ag sphere system embedded in free space ($n_4 = 1$). The expression in Eq. (13) is an incoherent sum of $|a_n|^2$ and $|b_n|^2$, which are the squared moduli of the electric and magnetic multipoles of order 2^n, respectively. Therefore, we can perform a direct multipolar decomposition of Q_{sca} in order to isolate the respective contributions of the electric and magnetic dipole ($n = 1$), quadrupole ($n = 2$), and octopole ($n = 3$). Since the middle dielectric layer is thin and has a small refractive index ($n_{SiO_2} \approx 1.5$) we expect the magnetic multipoles to be weak and the electric multipole contributions to dominate the overall scattering lineshape.

We therefore focus our analysis only on the electric multipole (a_n) contributions and subsequently validate this assumption by direct comparison with the fully multipolar solution. Using Eq. (13) with realistic dispersion data for SiO_2[21] and Ag[22], we plot in Figs. 2(a) and (b) the scattering efficiencies computed considering the first three electric multipoles separately and the total (N=10) multipolar scattering efficiencies for a compact Ag sphere and for the Ag-SiO_2-Ag system with the same dimension, respectively. We appreciate that the Ag-SiO_2-Ag system is designed to display two notable features that are not present in the case of the compact sphere. First, there appears a Fano-like dipole resonance at $\omega = 2{*}10^{15}$ rad/s and, second, we observe a small electric quadrupole peak at $\omega = 3.19 * 10^{15}$ rad/s.

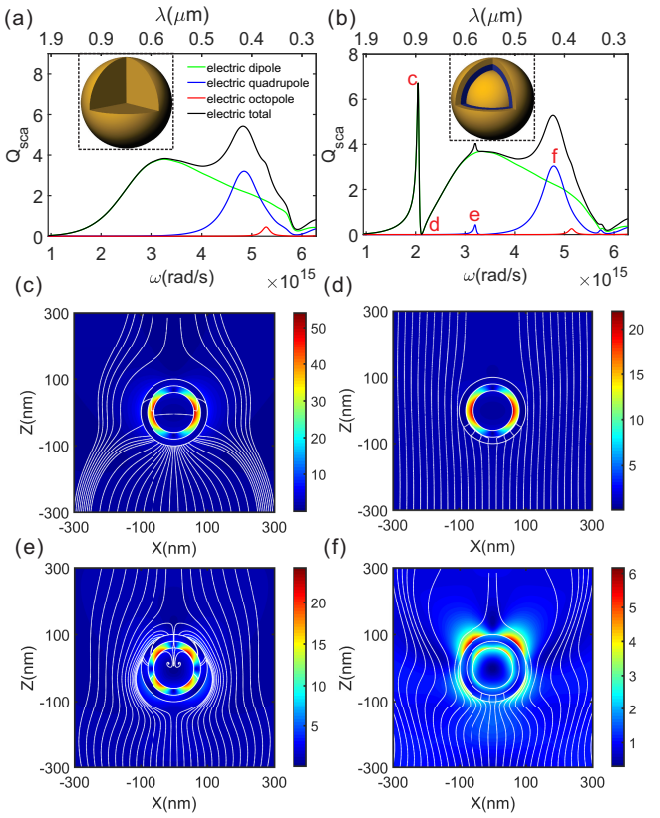

FIG. 2. The first three electric multipoles and the total electric scattering efficiencies of (a) the compact silver sphere with radius r=100 nm and (b) the single three-layered sphere with r_1=60 nm and $d_2 = d_3$=20 nm. The electric field amplitude $|E|$ distributions are plotted at (c) the scattering peak near the antiresonance position, (d) the antiresonance position, (e) the small electric quadrupole peak position, (f) the large electric quadrupole peak position. These positions are indicated by c-f in (b). The white streamlines are tangential to the Poynting vector with arrows indicating the Poynting vector directions

In order to better understand the behavior of these resonances we show in Figs. 2(c)-(f) the computed electric field amplitude $|E|$ along with the streamlines of the Poynting vector (in white) corresponding to the resonant frequencies of the Ag-SiO_2-Ag system. The field distributions are obtained using the series expansion formulas using Eqs. (1)-(6) once the Lorenz-Mie coefficients are computed.[18] The peak positions are labeled in panel (b) according to the field distributions shown in the corresponding panels below. The field shown in panel (c) corresponds to the resonant frequency labeled by c in panel (b) and features the maximum of the scattering efficiency, which is due to a dipolar resonance with a narrow frequency width. The frequency and corresponding wavelength scales are also shown in panels (a) and (b). In

this case the electric field has a distinctive dipolar nature and is strongly confined in the middle dielectric layer. However, the Poynting vector streamlines are strongly perturbed by the presence of the Ag-SiO_2-Ag system, which indicates strong scattering. In particular, the field distribution shown in panel (d) corresponds to the excitation of a dipolar antiresonance (position d in panel (b)) where the scattering is completely suppressed. Such an antiresonance behavior is a general phenomenon in coupled-oscillator physics where a pronounced minimum in the amplitude of one oscillator of a coupled system at a particular frequency is accompanied by a large shift in its oscillation phase. Antiresonances are caused by destructive interference of different channels, for example between an external driving force and the interaction with another oscillator, and are the underlying physical mechanism behind Fano-type lineshapes. At the antiresonance frequency, the electric field is strongly confined inside the middle dielectric layer and shows a characteristic dipole distribution. At this frequency, the light incident directly upon the sphere is absorbed (no Poynting vector streamlines are present beyond the target), while the adjacent streamlines pass the object undeflected, which is the typical behavior of non-scattering structures.[18] In panel (e) we show the field distribution corresponding to the electric quadrupole peak labeled by e in panel (b). A characteristic quadrupolar field pattern can now be observed strongly concentrated on the surface of the inner metallic core. Finally, in panel (f) we show the field distribution corresponding to the electric quadrupole peak labeled by f in panel (b). The quadrupolar field pattern is visible largely confined on both the Ag core and the outer Ag shell surfaces, where it shows the strongest confinement. Therefore, we can see that the excitation of electric quadrupoles at the inner and outer Ag layer surfaces is responsible for the electric quadrupole double-peak structure observed in the scattering spectra in Fig. 2(b). In the following section, we will show how these distinctive resonances can be understood and controlled through the pole-zero analysis of the electric dipole Lorenz-Mie scattering coefficients in the complex frequency plane.

IV. POLE-ZERO ANALYSIS

The quasi-static method has been often used to analyze the resonant behavior of core-shell nanospheres.[9,15,23,24] However, this method is only valid for spheres which are much smaller than the wavelength of light. In this section, we introduce the more general pole-zero analysis of the Lorenz-Mie coefficients of MDM spheres in the complex frequency plane. Since all the coefficients can be derived from full-wave vector Mie theory, the developed approach has no restrictions on wavelength or size parameter. Using this method, we investigate the connection between the geometric parameters of the multi-layered sphere system and the spectral positions of the complex zeros and poles of the Lorenz-Mie scattering coefficients. Through a systematic study of the character (i.e., real and imaginary parts) of the complex poles and zeros for different geometrical parameters and materials choices we can engineer Fano-like resonances over a desired spectral range. Furthermore, by properly tuning the geometrical parameters we demonstrate a novel scattering lineshape that originates from pole-zero-pole interaction. Finally, we show how the proposed method can be used to engineer the resonant behavior of the differential forward and backward scattering efficiencies.

A. Introduction to the pole-zero method

Pole-zero diagrams are widely used to help understand the the transfer function properties in control systems,[25] and have also been used to explain dipolar Fano-like resonances in finite nanoparticle clusters in the quasi-static regime.[9] In our full-vector analysis, we regard the Lorenz-Mie coefficient a_n in Eq. (7) as the rational response function of the oscillation modes associated to each multipolar order. When inserted in Eq. (13) they provide the scattering response function of the multi-layered sphere under plane wave excitation. Therefore we perform a systematic pole-zero analysis of the multipolar Lorenz-Mie coefficients in order to understand the resonant and antiresonant (i.e., pole-zero proximity) behavior of MDM spheres in the complex frequency plane.

We will first focus on the pole-zero analysis of the a_1 Lorenz-Mie scattering coefficient. Specifically, we consider the complex frequency $\tilde{\omega} = \omega' + i\omega''$ where the real part ω' approximately corresponds to the real excitation frequency of a resonant mode by an incident electromagnetic wave and the imaginary part ω'' corresponds to the decay rate of the excited resonance. A large imaginary part represents a lossy scattering resonance with a broad spectrum, while resonances (i.e. poles) with small imaginary parts describe high-quality resonances. Likewise, all wave numbers appearing in Eq. (7) will now be extended to the complex plane. In the case of a single sphere the complex frequencies introduced above are known as its natural oscillation frequencies, or virtual frequencies due to their complex nature.[18,26] We obtain all the complex zeros and poles of a_1 from Eq. (7) by sweeping the complex frequency plane in order to find the local minima of the expressions appearing in the numerator and denominator, respectively. We will show in the next section that the knowledge of the complex zeros and of the complex poles of the system enables, for any choice of structural parameters, the control of the spectral lineshapes of the resulting optical efficiencies.

B. Pole-zero analysis of Q_{sca}

We now show how varying the geometrical parameters of the Ag-SiO_2-Ag nanosphere affects the poles and zeros of the a_1 Lorenz-Mie coefficient and how the pole-zero

diagrams in the complex frequency plane are very useful tools for the engineering of the scattering lineshapes of multi-layered nanoparticles.

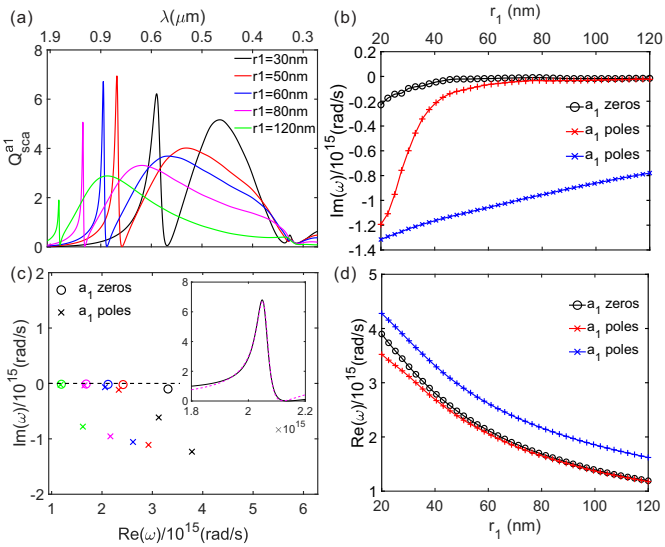

FIG. 3. (a) The electric dipole scattering efficiencies with respect to different r_1. (b) The imaginary parts of a_1 zero and a_1 poles as functions of r_1. (c) Pole-zero diagram of a_1 for various r_1. Colors correspond to the curves in (a). The Inset shows the Fano lineshape fitting curve (black solid line) and the electric dipolar scattering efficiency (magenta dashed line) when r_1=60 nm in (a). Figs. 3(a) and (c) share the same frequency axis. (d) The real parts of a_1 zero and poles as functions of r_1.

Fig. 3(a) shows the electric dipole scattering efficiencies ($Q^{a_1}_{sca}$) for several values of r_1 and $d_2 = d_3 = 20$ nm. When r_1 becomes larger than 60 nm, a Fano-like asymmetric lineshape appears in the spectrum. The origin of this Fano-like resonance can be understood by looking at the pole-zero digram that we computed and showed in Fig. 3(c) for different values of r_1. For each r_1 there corresponds one zero (circles) and two poles (crosses) in the complex frequency plane. The zero always has a small imaginary part compared to the real part, leading to a dip in the scattering spectrum. As r_1 increases, the zero shifts to smaller frequencies (red-shift) and one of the poles moves towards the zero of a_1. When the pole starts to overlap with the zero, a distinctively asymmetric Fano-like lineshape appears in spectrum of the scattering efficiency of the system. On the other hand, the second pole retains a large imaginary part and does not interact with the other pole or zero. Its large imaginary part is characteristic of a lossy scattering resonance, which corresponds to the broad scattering lineshape that is visible at larger frequencies in the spectrum of Fig. 3(a). In order to better characterize the observed resonances in the complex frequency plane we performed a systematic analysis of the positions of the imaginary and real parts of the complex poles and zeros with respect to r_1, as illustrated in Figs. 3(b) and (d), respectively.

In particular, Fig. 3(b) clearly shows that when r_1 approaches the value of 60 nm, the imaginary part of one of the two poles (red line with crosses) comes in close proximity with the one of the zero (black line with circles). On the other hand, we see in Fig. 3(d) that under the same conditions also the real parts of the same zero and pole are brought to almost coincidence, thus giving rise to a strongly asymmetric and sharp scattering resonance. Moreover, the resonant lineshapes of $Q^{a_1}_{sca}$ that originate from the pole-zero overlap can be modeled using the classical Fano lineshape equation:[27]

$$Q^{a_1}_{sca} = A\frac{(F\gamma + \omega - \omega_0)^2}{(\omega - \omega_0)^2 + \gamma^2} \tag{19}$$

where A is a scaling factor, F is the asymmetric parameter determined by the phase change across the transition, ω_0 is the position of the resonance that in our approach corresponds to the real part of pole-zero pair, and γ is the width of the decay rate corresponding to the imaginary part of the complex frequency in the pole-zero pair. In the Inset of Figure 3(c) we show a representaive spectrum of the electric dipolar scattering efficiency $Q^{a_1}_{sca}$ for the pole-zero overlap condition (magenta dashed line) along with the Fano lineshape fitting curve (black solid line) obtained with the parameters derived from the complex pole-zero overlap condition. The two lineshapes are overlapping around the resonant frequency, which demonstrates the Fano-like nature of the pole-zero dipolar interaction in the considered system.

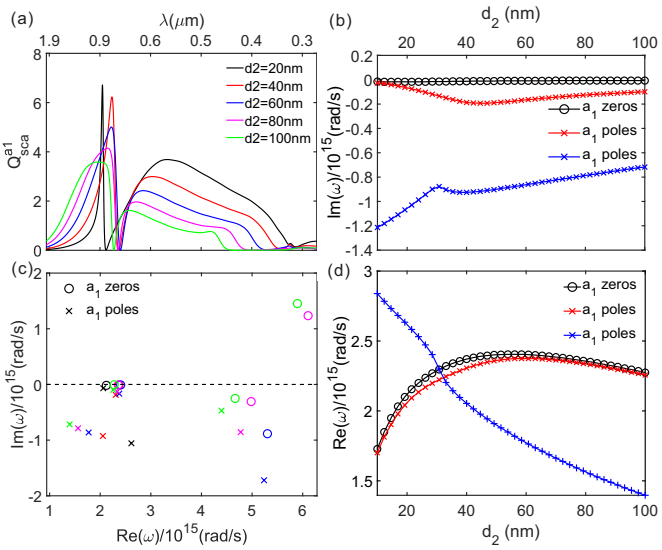

FIG. 4. (a) The electric dipole scattering efficiencies for different d_2. (b) The imaginary parts of zero and poles as functions of d_2. (c) The pole-zero diagram of a_1 for various d_2. The colors correspond to curves in (a). Figs. 4(a) and (c) share the same frequency axis. (d) The real parts of zero and poles as functions of d_2.

In order to achieve a complete characterization of the Fano-like behavior we compute $Q^{a_1}_{sca}$ as a function of d_2

for the fixed values $r_1 = 60$ nm and $d_3 = 20$ nm and show our results in Fig. 4(a). Strongly dispersive Fano-like resonance lineshapes are clearly observed. These lineshapes are understood looking at the corresponding complex frequency pole-zero diagram shown in Fig. 4(c), where there appear again two poles and one zero for each value of d_2 in the interested Fano-like lineshape region. In this case, when d_2 is larger than 40 nm, the imaginary part of the pole nearest to the zero increases and the pole moves away from the zero. As the pole-zero separate with respect to their imaginary parts by varying d_2, as shown in Fig. 4(b), the sharp Fano-like asymmetric lineshape evolves into a broader one with reduced amplitude variation. In particular, Figs. 4(b) and (d) show that the difference in both the real and the imaginary parts of the pole (red line with crosses) and the zero (black line with circles) increases when d_2 becomes larger than 20 nm. Interestingly, the real parts begin to approach each other again when d_2 becomes larger than approximately 60 nm, though the separation of the imaginary parts remains large preventing the formation of sharp Fano-like resonances.

Next we compute $Q_{sca}^{a_1}$ as a function of d_3 when r_1=60 nm and d_2=20 nm are kept constant. The results of our analysis are shown in Fig. 5(a). We notice that when d_3=20 nm the scattering spectrum features the Fano-like asymmetric lineshape. However, as d_3 is increased to 40 nm, a novel and strongly dispersive lineshape appears in the spectrum. An enlarged view of this lineshape is shown in the inset in the figure. The blue dots in the inset correspond to the total (multipolar) Q_{sca} which nearly perfectly overlaps with $Q_{sca}^{a_1}$ in the interested frequency range. This shows that controlling the scattering efficiency at the dipolar level ($Q_{sca}^{a_1}$) enables the engineering of even more complex lineshapes in Q_{sca}. By further increasing d_3, the resonant dip will be drastically reduced, as it is the case in the spectrum obtain for d_3=60 nm.

In order to unveil the nature of this novel asymmetric lineshape we analyze the pole-zero diagram in the Fig. 5(c). We notice that when $d_3 = 40$ nm a pole-zero-pole interaction occurs where the red pole-zero pair overlaps in the real frequency axis with a second (red) pole with a large imaginary frequency component. From the results shown in Figs. 5(b) and (d) we can see that the pole (red line with crosses) and the zero (black line with circles) strongly interact when $d_3 > 20$ nm. Moreover, the imaginary part of the other pole (blue line with crosses) overlaps with the pole-zero pair when $d_3 \approx 35$ nm as seen in Fig. 5(d), leading to the new three-channel interaction (pole-zero-pole). In this case, a pole corresponding to a lossy resonance will be excited at the same real frequency of a pole-zero interaction, which creates a distinctively asymmetric lineshape in both $Q_{sca}^{a_1}$ and Q_{sca}. If we further increase d_3 to d_3 >50 nm only one pole remains visible, in agreement with the familiar case of a compact large metallic sphere. In the inset of Fig. 5(c) we plot the electric field distribution $|E|$ at the frequency corresponding to the minimum of Q_{sca}, which is obtained

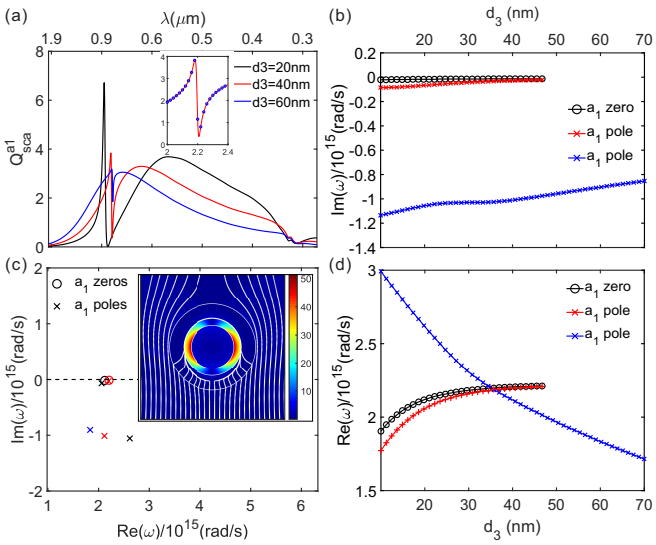

FIG. 5. (a)The electric dipole scattering efficiencies with respect to different d_3, the inset shows a zoom-in view of Q_{sca} for d_3= 40 nm at the superposition position of the novel asymmetric lineshape. (b)The imaginary parts of the zero and the poles as functions of d_3. (c) The pole-zero diagram of scattering efficiencies shown in (a) on the complex plane, the colors are identical to (a) for different d_2, the inset shows the electric field $|E|$ at the antiresonance position for d_3= 40 nm. Figs. 5(a) and (c) share the same frequency axis. (d) The real parts of the zero and the poles as functions of d_3.

for $d_3 = 40$ nm. This field distribution shows a dipolar character in close analogy with the results previously shown in Figs. 2 (c) and (d). However, in this case the involvement of the lossy pole prevents the antiresonance condition of zero scattering, which is also consistent with the more significant perturbation of the Poynting vector streamlines around the particle. We believe that the strongly dispersive nature of this multi-channel resonance in combination with the pole-zero engineering approach provides novel opportunity for applications to active plasmonic devices and scattering sensors.

C. Pole-zero analysis of Q_{bs} and Q_{fd}

In this section we will discuss the applicability of our method to the control of differential scattering quantities. When considering the engineering of Q_{sca} it is clear that the various multipole terms all contribute independently without interference. On the other hand, in the case of the differential scattering efficiencies for back-scattering Q_{bs} and forward-scattering Q_{fd}, defined in Eqs. (16) and (17), the various multipole terms interfere coherently, generally making the resulting lineshapes more complicated. Nonetheless, Fano-like resonances have been found in the spectra of plasmonic nanostructures for both Q_{bs} and Q_{fd} as a result of the interference of different radiation modes.[27–29] Though the presence of

Fano resonances in these spectra can be understood using the well-established mode hybridization theory,[30,31] the engineering of Fano lineshapes in more general multilayered systems poses significant challenges. Recently, theoretical work that uses auxiliary eigenproblem formulations with material-dependent spectral parameters has been introduced and successfully utilized in relation to the optical cloaking of core-shell (two-layers) spheres.[32] This method enables a systematic study of the effect of the cloaking material's properties on back-scattering and forward-scattering differential cross sections. However, the development of an accurate and scalable methodology that is suitable for the engineering of Q_{bs} and Q_{fd} in complex systems with multiple geometrical and materials degrees of freedom remains a very difficult task. Here we show that a direct pole-zero approach can be utilized to efficiently design desired forward- and back-scattering properties over a wide range of geometrical and materials parameters.

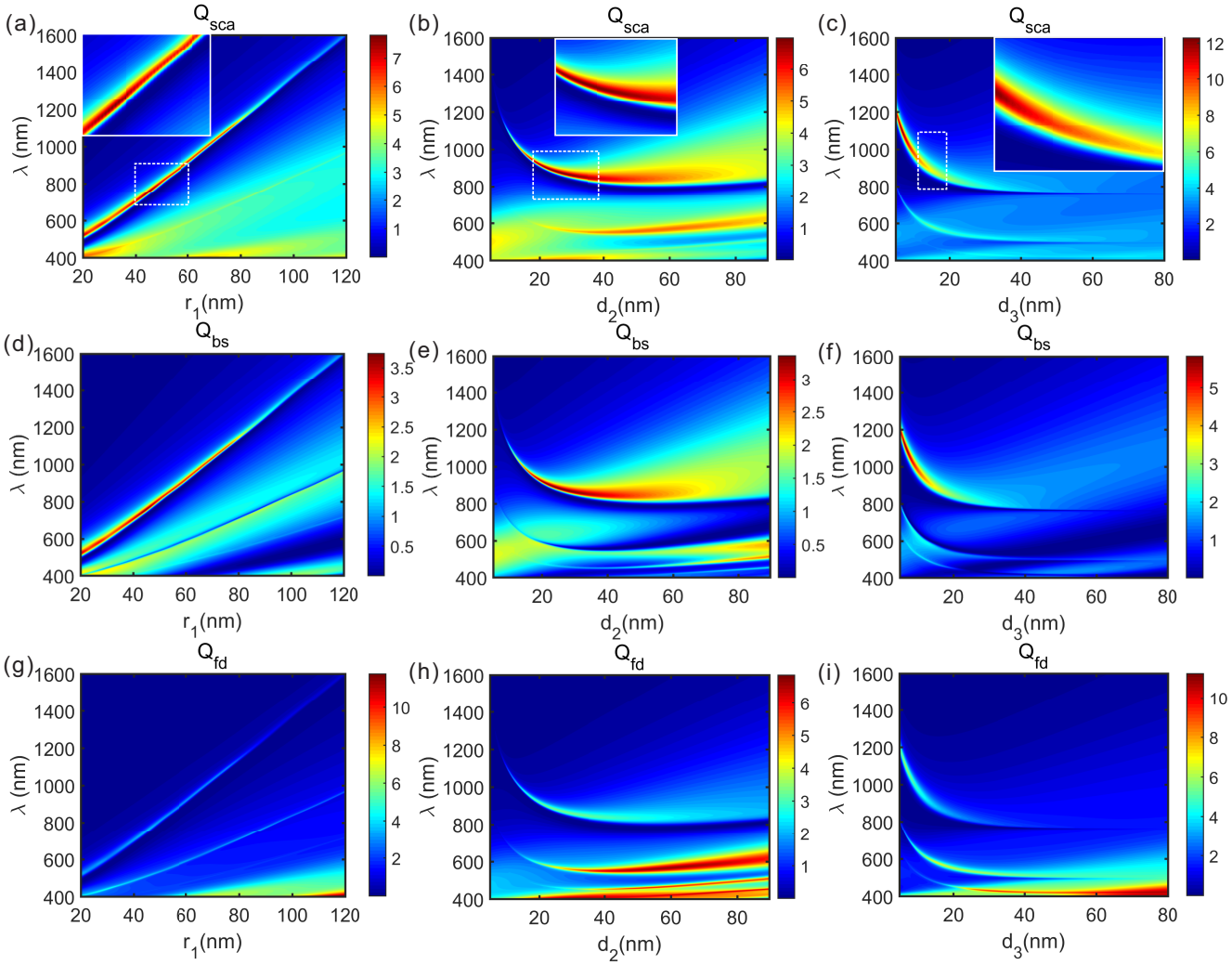

FIG. 6. (a),(d),(g) are the total scattering efficiency Q_{sca}, the back-scattering efficiency Q_{bs}, and the forward-scattering efficiency Q_{fd} respectively as a function of r_1 with d_2=20nm, d_3=20 nm. (b),(e),(h) are the same efficiencies as a function of d_2 with r_1=60 nm and d_3=20 nm. (c),(f),(i) are the same efficiencies as a function of d_3 with r_1=60 nm and d_2=40 nm.

In Fig. 6 we display the multipolar Q_{sca}, Q_{bs}, and Q_{fd} computed with respect to the geometrical parameters r_1, d_2, and d_3. We focus first on panels (a)-(c) that show Q_{sca} in a large parameter range. Two main resonances are visible in these plots and correspond to the dipolar and the quadrupolar modes of the structures. The resonance that appears at longer wavelengths corresponds to a dipole mode asymmetric Fano-like lineshape, as dis-

cussed in previous sections. An expanded view of this resonance is shown in the inset, where we can observe clearly its antiresonance nature with a zero scattering region. A quadrupole resonance is observable for shorter wavelengths. Panels (d)-(f) and (g)-(i) show Q_{bs} and Q_{fd}, respectively. These quantities also feature an asymmetric Fano lineshape at the dipole mode position as in the case of Q_{sca}. However, at the quadrupole resonance, Q_{fd} displays a peak while Q_{bs} features a pronounced dip. In order to better understand these results we consider mutlipolar pole-zero analysis of Q_{bs} and Q_{fd}.

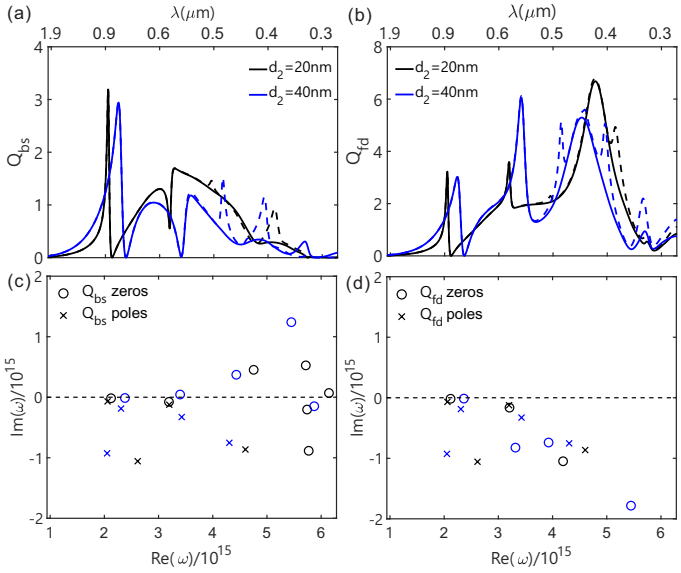

FIG. 7. (a) The total back-scattering efficiencies (dashed line) and the back-scattering efficiencies computed using a_1 and a_2 only (solid lines), (b) the total forward-scattering efficiencies (dashed line) and the forward-scattering efficiencies computed using a_1 and a_2 only (solid lines), (c) and (d) are the pole-zero diagrams for back-scattering and forward-scattering efficiencies respectively calculated using only a_1, a_2 with color indicating identical d_2 as in (a) and (b).

In order to include only the necessary multipoles in our pole-zero analysis we first compared the spectra of Q_{bs} and Q_{fd} obtained using the full multipolar Mie theory and the $Q_{bs}^{(a_1,a_2)}$ and $Q_{fd}^{(a_1,a_2)}$ obtained by retaining only the first two multipolar orders. The results shown in Fig. 7 by the solid lines are contributed only by the two electric modes a_1 and a_2. The agreement with the full multipolar theory is excellent around the spectral regions where the Fano-like resonances appear, fully justifying a two-multipole pole-zero approach. Therefore, expressing Eqs. (16) and (17) in fractional form limited to only two electric modes we can obtain the following equations for the differential scattering efficiencies:

$$\begin{aligned} Q_{fd}^{(a_1,a_2)} &= \frac{1}{(k_0 r_m)^2}|3a_1 + 5a_2|^2 \\ &= \frac{1}{(k_0 r_m)^2}\left|\frac{3a_1^n a_2^d + 5a_2^n a_1^d}{a_1^d a_2^d}\right|^2 \end{aligned} \tag{20}$$

$$\begin{aligned} Q_{bs}^{(a_1,a_2)} &= \frac{1}{(k_0 r_m)^2}|-3a_1 + 5a_2|^2 \\ &= \frac{1}{(k_0 r_m)^2}\left|\frac{-3a_1^n a_2^d + 5a_2^n a_1^d}{a_1^d a_2^d}\right|^2 \end{aligned} \tag{21}$$

where we denote by a_1^n, a_1^d, a_2^n, and a_2^d the numerator of a_1, the denominator of a_1, the numerator of a_2, and the denominator of a_2, respectively. Since a scalar constant does not affect the lineshapes, we set $k_0 r_m = 1$ and study the numerator and denominator of Eqs. (20) and (21) in order to obtain their complex zeros and poles.

In Fig. 7(a) and (b) we plot respectively Q_{bs}, $Q_{bs}^{(a_1,a_2)}$ and Q_{fd}, $Q_{fd}^{(a_1,a_2)}$ of the Ag-SiO_2-Ag sphere when varying d_2 with $r_1 = 60$ nm and $d_3 = 20$ nm. The corresponding pole-zero diagrams are presented in Fig. 7(c) and (d). We can clearly observe that the Fano-like lineshape at $Re(\omega) \approx 2.2 * 10^{15}$ corresponds to the proximity of a zero and a pole. The pole-zero diagram also explains the dip in Q_{bs} and the peak in Q_{fd} at the quadrupole resonance near $Re(\omega) \approx 3.2 * 10^{15}$. For $d_2 = 20$ nm, Q_{bs} has a pole-zero pair with the zero nearer to the real axis, resulting in a dip in the efficiency. On the other hand, Q_{fd} has a pole-zero pair with the pole closer to the real axis, resulting in a small peak instead. These features are more evident for d_2=40 nm where Q_{bs} has a zero near the real axis and far from the pole, resulting in a spectral dip that goes to zero. For Q_{fd} the pole is closer to the real axis and far from the zero, leading to the onset of a large peak at the quadrupole mode position.

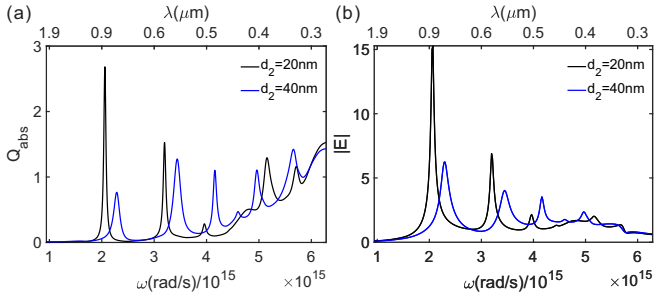

FIG. 8. (a) The absorption cross sections and (b) the averaged electric field amplitude of the middle dielectric layer for Ag-SiO_2-Ag spheres with the same r_1, d_2, and d_3 in Fig. 7.

Using the same geometric parameters as in Fig. 7, we also calculate the absorption efficiency Q_{abs} and plot it in Fig. 8(a). We observe a spectrally narrow resonant lineshape in the absorption efficiency corresponding to the antiresonance position of the scattering efficiency. A better understanding of these peaks is obtained by plotting the average electric field amplitude $|E|$ within the SiO_2 layer as in Fig. 8(b). The peaks of Q_{abs} correspond to a large $|E|$ concentration and enhancement (up to 15x) within the middle layer of the structure, as shown in Figs. 2(c) and (e). Since the antiresonance position can be engineered by tuning the sphere geometry, the absorption efficiency position can likewise be engineered. This fea-

ture makes the Ag-SiO_2-Ag (or more generally the MDM spherical systems) ideal candidates for realizing metamaterials with tunable absorption. Moreover, the spectral design Q_{bs} and Q_{fd} antiresonances with large absorption enhancement could be utilized for the engineering of more efficient detectors with nanoscale footprints. Finally, due to the strong field concentration and enhancement within the dielectric layer, this system could alternatively function as an efficient emitter with an appropriate active material embedded in the dielectric layer.

In the next section we will demonstrate the flexibility of the pole-zero analysis by applying it to the study of the scattering resonances of the Au-SiO_2-Au as well as the fully dielectric Si-SiO_2-Si three-layered sphere system.

D. MDM sphere and n_{high}-n_{low}-n_{high} whole dielectric sphere pole-zero analyses

In the previous sections we analyzed the Ag-SiO_2-Ag system and showed that asymmetric Fano-like resonances originate from the interaction of complex poles and zeros of the Lorenz-Mie coefficient a_1. The picture of the Fano-like resonance effect is generally valid for a concentric spheres geometry and does not depend on the specific choice of the materials. In particular, our analysis of the scattering resonances and the associated local field distribution shows that the pole-zero pair corresponds to the excitation of a plasmonic gap resonance where the electric field is strongly localized inside the dielectric region of the MDM system. In addition, we have shown that by tuning d_3 it is possible to engineer a novel asymmetric Fano-like resonance by controlling the position of an additional pole with large imaginary part. In order to demonstrate the general nature of this picture we will now consider the case of a Au-SiO_2-Au three-layered sphere.

In Fig. 9(a) we show the $Q_{sca}^{a_1}$ for different values of d_3 with fixed $r_1 = 60$ nm and $d_2 = 25$ nm. We observe that when d_3=20 nm, a Fano-like resonance appears in agreement with the pole-zero interaction visible in Fig. 9(c) However, when d_3=30 nm the perturbation induced by the other complex pole starts to significantly affect the Fano-like lineshape, similarly to the situation previously discussed for the Ag-SiO_2-Ag system. However, when d_3 becomes too large then the presence of the middle dielectric layer can be neglected resulting in only one lossy pole (i.e. the pole with large imaginary part) as shown in Fig. 9(c) for the case of d_3= 60nm. We notice that the pole-zero behavior as a function of the parameter d_3 in Figs. 9(b) and (d) is very similar to the one previously discussed for the Ag-SiO_2-Ag system. It is clear from this analysis that Fano-like lineshapes can be largely controlled in general MDM concentric-sphere systems by appropriately shifting the frequency position of complex poles and zeros through the variation of the geometrical parameters r_1, d_2, d_3.

Finally, we apply the pole-zero analysis to the case of an all- dielectric Si-SiO_2-Si system, which is characterized

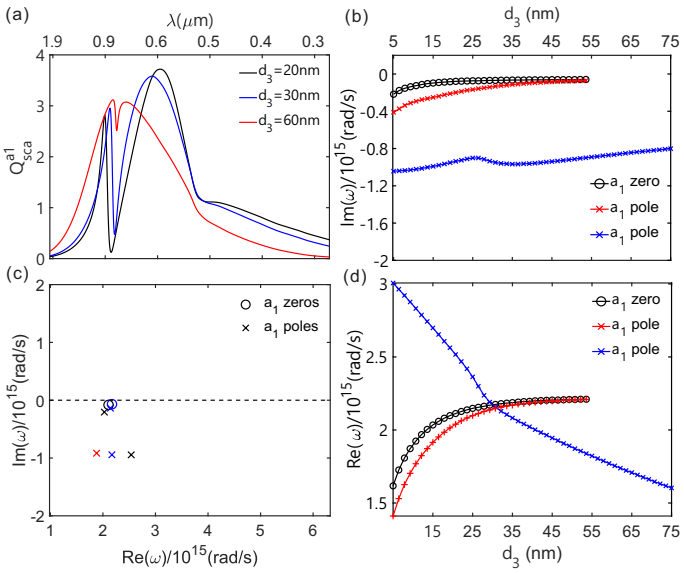

FIG. 9. (a) The electric dipole scattering efficiencies for various d_3 of the Au-SiO_2-Au sphere, where $r_1 = 60$ nm, $d_2 = 25$ nm. (b) The imaginary parts of a_1 zero and a_1 poles as functions of d_3. (c) The pole-zero diagram of a_1 for different d_3. Colors correspond to curves in (a). Figs. 9(a) and (c) share the same frequency axis. (d) The real parts of a_1 zero and poles as functions of d_3.

by lower absorption losses compared to its MDM counterpart. Moreover, high refractive index dielectric nanostructures exhibit strong magnetic responses.[33] Therefore, we study both the the dipolar electric (Q_{sca}^{a1}) and magnetic (Q_{sca}^{b1}) scattering efficiencies for the Si-SiO_2-Si system, which are shown in Figs. 10(a) and (b).

The scattering lineshape features a sharp anomalous transition region for the magnetic response of the system, as shown in panel (b), due to the excitation of Mie resonances.[18,33] It is evident that even in this case the pole-zero analysis is very instructive, as attested by the results in Figs. 10(c) and (d) showing the pole-zero diagram of the a_1 and b_1 Lorenz-Mie coefficients, respectively. In particular, we observe that for fully-dielectric multi-layered sphere systems there is no additional pole with large imaginary part in both pole-zero diagrams. This follows from the positive permittivity of Si and SiO_2 materials. However, for resonant dielectric systems we expect a larger number of poles and zeros compared to their MDM counterparts simply due to their larger size parameter, as visible in Figs. 10 (c) and (d). More importantly, also for fully-dielectric structures we observe anomalous scattering lineshapes due to complex pole-zero interactions. For instance, we see that at $\omega = 2.5 * 10^{15}$ rad/m the quantity Q_{sca}^{b1} features an asymmetric Fano-like lineshape, which is similar to what previously reported in the electric-type Lorenz-Mie coefficients of the MDM systems. The pole-zero diagram of b_1 is shown in Fig. 10(d), demonstrating a strong pole-zero interaction (i.e., strong overlap) at this frequency.

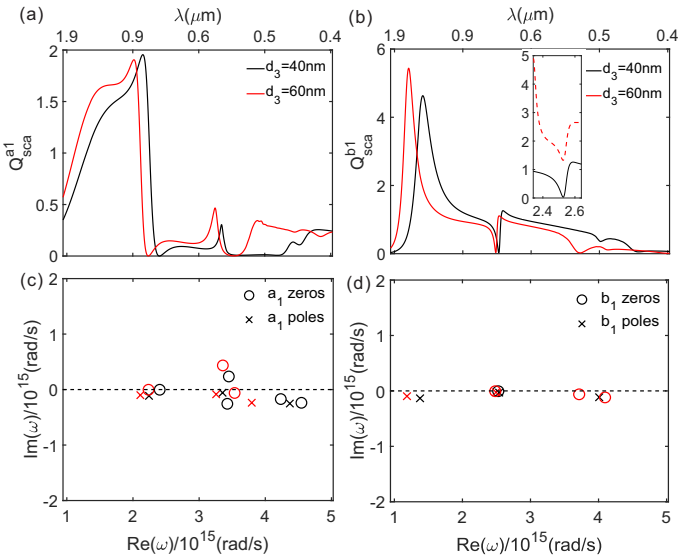

FIG. 10. (a) The electric dipole scattering efficiencies with respect to different d_3 of the Si-SiO_2-Si sphere, where $r_1 = 100$ nm, $d_2 = 100$ nm. (a) The magnetic dipole scattering efficiencies with respect to different d_3 for the same sphere. (c) The pole-zero diagram of a_1 for different d_3. Colors correspond to curves in (a). (d) The pole-zero diagram of b_1 for different d_3. Colors correspond to curves in (b).

The inset in Fig. 10(b) compares the multipolar (total) scattering efficiency (in red dashed-line) and the dipolar scattering efficiency Q_{sca}^{b1} (solid black line). We note that while the total efficiency values are larger due to the contributions of higher multipolar orders, a strongly dispersive and sharp lineshape also appears in total scattering as predicted by the pole-zero interaction at the magnetic dipole level. Therefore, the pole-zero method can be utilized to unambiguously identify and design both electric and magnetic anomalous scattering lineshapes.

V. CONCLUSIONS

In this work we used the full Mie theory solution of multi-layered spheres to rigorously investigate the anomalous scattering resonances of MDM and fully dielectric systems. In particular, these structures were found to exhibit controllable asymmetric Fano-like resonances that are explained as general pole-zero interactions in the complex frequency plane of both electric and magnetic dipole Lorenz-Mie coefficient. Moreover, for MDM systems we demonstrate a novel scattering lineshape that originates from a three-channel pole-zero-pole interaction. We also show how to control anomalous scattering resonances by shifting complex zeros and poles by varying the geometrical parameters of the systems. We further applied the pole-zero approach to the engineering of Q_{bs} and Q_{fd} where we considered the interference between different multipolar orders. While the examples presented in this paper are limited to three-layered spheres, our approach is general and can be naturally extended to multi-layered structures with any number of layers and materials. The engineering of strongly dispersive scattering and absorption resonances with controlled lineshapes in layered nanosphere structures provides unique opportunities for the demonstration of more efficient active devices including optical sensors, light emitters, and nonlinear optical elements with nanoscale footprints.

ACKNOWLEDGEMENT

This research was sponsored by the Army Research Laboratory and was accomplished under Cooperative Agreement Number W911NF-12-2-0023. The views and conclusions contained in this document are those of the authors and should not be interpreted as representing the official policies, either expressed or implied, of the Army Research Laboratory or the U.S. Government. The U.S. Government is authorized to reproduce and distribute reprints for Government purposes notwithstanding any copyright notation herein.

* dalnegro@bu.edu

[1] U. Fano, Physical Review **124**, 1866 (1961).
[2] M. W. Klein, T. Tritschler, M. Wegener, and S. Linden, Physical Review B **72**, 115113 (2005).
[3] D. Nau, A. Schönhardt, C. Bauer, A. Christ, T. Zentgraf, J. Kuhl, M. W. Klein, and H. Giessen, Physical review letters **98**, 133902 (2007).
[4] V. A. Fedotov, M. Rose, S. L. Prosvirnin, N. Papasimakis, and N. I. Zheludev, Physical review letters **99**, 147401 (2007).
[5] V. Fedotov, A. Tsiatmas, J. Shi, R. Buckingham, P. De Groot, Y. Chen, S. Wang, and N. Zheludev, Optics Express **18**, 9015 (2010).
[6] K. Bao, N. A. Mirin, and P. Nordlander, Applied Physics A **100**, 333 (2010).
[7] M. Gonçalves, A. Melikyan, H. Minassian, T. Makaryan, and O. Marti, Optics express **22**, 24516 (2014).
[8] B. Gallinet and O. J. F. Martin, Physical Review B **83**, 235427 (2011).
[9] C. Forestiere, L. Dal Negro, and G. Miano, Physical Review B **88**, 155411 (2013).
[10] F. Hao, Y. Sonnefraud, P. V. Dorpe, S. A. Maier, N. J. Halas, and P. Nordlander, Nano letters **8**, 3983 (2008).
[11] Z.-G. Dong, H. Liu, M.-X. Xu, T. Li, S.-M. Wang, J.-X.

Cao, S.-N. Zhu, and X. Zhang, Optics express **18**, 22412 (2010).
[12] M. J. Dicken, K. Aydin, I. M. Pryce, L. A. Sweatlock, E. M. Boyd, S. Walavalkar, J. Ma, and H. A. Atwater, Optics express **17**, 18330 (2009).
[13] Z. Samson, K. MacDonald, F. De Angelis, B. Gholipour, K. Knight, C. Huang, E. Di Fabrizio, D. Hewak, and N. Zheludev, Applied Physics Letters **96**, 143105 (2010).
[14] N. T. Fofang, N. K. Grady, Z. Fan, A. O. Govorov, and N. J. Halas, Nano letters **11**, 1556 (2011).
[15] F. Monticone, C. Argyropoulos, and A. Alù, Scientific reports **2**, 912 (2012).
[16] Y. Hu, S. J. Noelck, and R. A. Drezek, Acs Nano **4**, 1521 (2010).
[17] S. Mukherjee, H. Sobhani, J. B. Lassiter, R. Bardhan, P. Nordlander, and N. J. Halas, Nano letters **10**, 2694 (2010).
[18] C. F. Bohren and D. R. Huffman, *Absorption and scattering of light by small particles* (John Wiley & Sons, 2008).
[19] J.-M. Jin, *Theory and computation of electromagnetic fields* (John Wiley & Sons, 2011).
[20] A. A. R. Neves and D. Pisignano, Opt. Lett. **37**, 2418 (2012).
[21] D. Smith, E. Shiles, M. Inokuti, and E. Palik, Handbook of Optical Constants of Solids **1**, 369 (1985).
[22] P. B. Johnson and R. W. Christy, Phys. Rev. B **6**, 4370 (1972).
[23] X. Fan, W. Zheng, and D. J. Singh, Light: Science & Applications **3**, e179 (2014).
[24] T. J. Arruda, A. S. Martinez, and F. A. Pinheiro, Physical Review A **92**, 023835 (2015).
[25] R. C. Dorf and R. H. Bishop, *Modern control systems* (Pearson, 2011).
[26] J. A. Stratton, *Electromagnetic theory* (John Wiley & Sons, 2007).
[27] B. Luk'yanchuk, N. I. Zheludev, S. A. Maier, N. J. Halas, P. Nordlander, H. Giessen, and C. T. Chong, Nature materials **9**, 707 (2010).
[28] M. I. Tribelsky and B. S. Lykyanchuk, Physical review letters **97**, 263902 (2006).
[29] J. Yan, P. Liu, Z. Lin, H. Wang, H. Chen, C. Wang, and G. Yang, Acs Nano **9**, 2968 (2015).
[30] A. D. Khan, International Nano Letters **4**, 110 (2014).
[31] J. Qian, Y. Li, J. Chen, J. Xu, and Q. Sun, The Journal of Physical Chemistry C **118**, 8581 (2014).
[32] M. Pascale, G. Miano, and C. Forestiere, JOSA B **34**, 1524 (2017).
[33] A. García-Etxarri, R. Gómez-Medina, L. S. Froufe-Pérez, C. López, L. Chantada, F. Scheffold, J. Aizpurua, M. Nieto-Vesperinas, and J. J. Sáenz, Optics express **19**, 4815 (2011).